ADVANCED MATERIALS TECHNOLOGIES
www.advmattechnol.de

Elucidating the Bulk Morphology of Cellulose-Based Conducting Aerogels with X-Ray Microtomography

*Vasileios K. Oikonomou, Till Dreier, Alexandra Sandéhn, Mohsen Mohammadi, Jakob Lønborg Christensen, Klas Tybrandt, Anders Bjorholm Dahl, Vedrana Andersen Dahl, Martin Bech, and Eleni Stavrinidou**

Conducting cellulose composites are promising sustainable functional materials that have found application in energy devices, sensing and water purification. Herein, conducting aerogels are fabricated based on nanofibrillated cellulose and poly(3,4-ethylenedioxythiophene) polystyrene sulfonate, using the ice templating technique, and their bulk morphology is characterized with X-ray microtomography. The freezing method (−20 °C in a freezer vs liquid nitrogen) does not impact the mean porosity of the aerogels but the liquid-N_2 aerogels have smaller pores. The integration of carbon fibers as addressing electrodes prior to freezing results in increased mean porosity and pore size in the liquid-N_2 aerogels signifying that the carbon fibers alter the morphology of the aerogels when the freezing is fast. Spatially resolved porosity and pore size distributions also reveal that the liquid-N_2 aerogels are more inhomogeneous. Independent of the freezing method, the aerogels have similar electrochemical properties. For aerogels without carbon fibers, freezer-aerogels have higher compression modulus and are less stable under cycling compression fatigue test. This can be explained by higher porosity with larger pores in the center of liquid-N_2 aerogels and thinner pore walls. This work demonstrates that micro-CT is a powerful tool for characterizing the morphology of aerogels in a non-destructive and spatially resolved manner.

1. Introduction

Due to the need for eco-friendly solutions to tackle the world's growing technological demands, renewable biomaterials are combined with synthetic materials to form composite systems with desired properties. Cellulose is the most abundant biopolymer on earth as it represents the highest percentage of plant biomass. The most common source of cellulose is wood, in the form of wood pulp[1] however, cellulose is also produced by bacteria, algae, and fungi.[2] Materials based on cellulose have been widely used traditionally in paper[3] and textile[4] industries. In recent years non-traditional uses of cellulose have emerged due to the need to reduce the environmental footprint of technological materials by minimizing electronic[5] and plastic wastes.[6,7] Furthermore, cellulose has attractive properties for technological purposes, such as non-toxicity,

V. K. Oikonomou, A. Sandéhn, M. Mohammadi, K. Tybrandt, E. Stavrinidou
Laboratory of Organic Electronics
Department of Science and Technology
Linköping University
Norrköping SE-60174, Sweden
E-mail: eleni.stavrinidou@liu.se

V. K. Oikonomou, A. Sandéhn, M. Mohammadi, K. Tybrandt, E. Stavrinidou
Wallenberg Wood Science Center
Department of Science and Technology
Linköping University
Norrköping SE-60174, Sweden

T. Dreier, M. Bech
Department of Medical Radiation Physics
Clinical Sciences Lund
Lund University
SE-22242 Lund, Sweden

T. Dreier
Excillum AB
Stockholm SE-16440, Sweden

J. L. Christensen, A. B. Dahl, V. A. Dahl
Department of Applied Mathematics and Computer Science
Technical University of Denmark
Richard Petersens Plads, Kongens Lyngby DK-2800, Denmark

E. Stavrinidou
Umeå Plant Science Centre
Department of Forest Genetics and Plant Physiology
Swedish University of Agricultural Sciences
Umeå SE-90183, Sweden

The ORCID identification number(s) for the author(s) of this article can be found under https://doi.org/10.1002/admt.202300550

DOI: 10.1002/admt.202300550

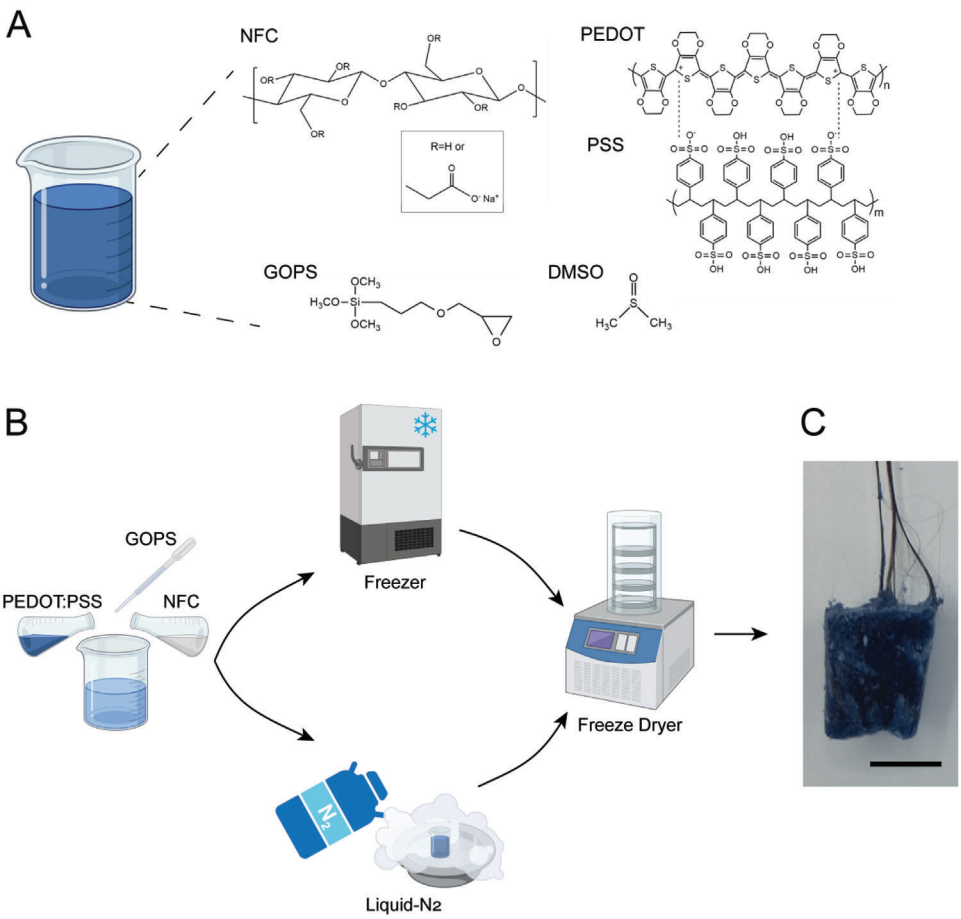

Figure 1. Conducting aerogel components and fabrication process. A) Chemical structures of PEDOT:PSS, nanofibrillated cellulose (NFC), GOPS, and DMSO. B) Fabrication process schematic, PEDOT:PSS, NFC, and GOPS mixture is frozen with two different methods, at −20 °C in a freezer and flash frozen with liquid-N_2. The frozen mixture in a mold is then placed in a freeze dryer to form the aerogel. C) Photograph of the aerogel with embedded carbon fibers (scale bar: 1 cm).

biodegradability, good mechanical properties, interesting optical characteristics, and compatibility for modification with various synthetic materials.[8]

Cellulose properties arise from its chemical structure. Cellulose is a polymer formed by D-glucose repeating units, covalently linked together by β-1-4 glycosidic bonds.[9] On each glucose unit, there are three hydroxyl groups that contribute to the hydrophilicity of cellulose but also favor the formation of multiple hydrogen bonds among adjacent polymer chains. The chains are thus firmly bound together resulting in the formation of microfibrils that exhibit high tensile strength.[10] Cellulose fibrils can be treated chemically and mechanically to produce nanofibrillated cellulose (NFC) that consists of nano-sized fibrils with diameters of less than 20 nm and varying lengths up to several micrometers. There are several examples in the literature where cellulose is combined with synthetic materials[11,12] such as inorganic nanoparticles,[13] ionic liquids,[14] carbon nanotubes,[15] and conducting polymers[16] for applications in non-traditional areas such as energy[17] and biomedical devices,[18] water treatment,[19] optical metamaterials,[20,21] and smart textiles.[22,23]

Specifically, the conducting polymer poly(3,4-ethylenedioxythiophene) polystyrene sulfonate (PEDOT:PSS), has been widely used in composites with cellulose[16] due to its high electronic and ionic conductivity,[24] high specific capacitance, and thermoelectric properties enabling the formation of active materials for supercapacitors,[25–30] thermoelectric generators,[31] sensors,[32] and actuators.[33] PEDOT:PSS is processed from an aqueous solution and therefore can be directly mixed with cellulose pulp or more refined forms of cellulose such as NFC to form functional composites with paper-like structures or even 3D porous aerogels. Computational microscopy together with X-ray scattering studies revealed that PEDOT:PSS organizes along cellulose fibers resulting in bead-like structures due to pi–pi stacking interactions between the PEDOT chains.[29,34–36] PEDOT:PSS-NFC aerogels in particular are formed via the ice template method resulting in conducting aerogels with enhanced mechanical properties. These aerogels have been applied for multiparameter sensors[32,37] that enable monitoring of temperature, humidity, and pressure in a single device and as a solar steam generator for water purification.[38] So far their morphology and porosity have been characterized with scanning electron microscopy that, although has good resolution, it gives information only for the sections under inspection.[32,37,38] Mercury porosimetry on the other hand can

give information on the pore size distribution and total pore surface and has been used to characterize PEDOT aerogels without cellulose. However, this method is destructive for the sample and does not give any information on the spatial distribution of the pores as the whole aerogel is treated as one volume.[39,40]

In this work, we developed conducting aerogels based on cellulose nanofibrils and PEDOT:PSS and characterized their bulk morphology with X-ray microtomography. The aerogels morphology was assessed in 3D in a non-destructive way and hence we were able to evaluate the pore size distribution and overall porosity and how they vary within the full volume. We investigated the effect of the freezing method on the aerogel's morphology and further assessed how the incorporation of carbon fibers as addressing electrodes impacted the structural organization. Finally, we characterized the electrochemical and mechanical properties of the aerogels produced with the different freezing methods.

2. Results

PEDOT:PSS-NFC aerogels were fabricated using the ice templating method. Briefly, NFC was mixed with PEDOT:PSS and the thermal crosslinker glycidoxypropyl trimethoxysilane (GOPS), and the mixture was homogenized with mechanical stirring **Figure 1**A. The mixture was then poured into molds and frozen with two different methods: i) at −20 °C for 24 h in a freezer and ii) flash frozen with liquid N_2 (Figure 1B). The frozen solutions were then placed in a freeze dryer that removed the ice crystals via sublimation that are formed between the solutes, resulting in 3D porous aerogels. The water stability of the aerogels was enhanced due to the addition of the GOPS crosslinker. Upon thermal annealing of the aerogel, the epoxy groups in GOPS react with the hydroxyl groups present in PSS and NFC.[41] The PEDOT:PSS-NFC aerogels were also treated with dimethyl sulfoxide (DMSO) vapor to enhance their electronic conductivity as DMSO acts as a secondary dopant for PEDOT:PSS[37] In some of the aerogels, bundles of carbon fibers were added to the mixture prior to freezing that can act as addressing electrodes.

First, the bulk morphology of the porous aerogels was characterized with X-ray microtomography. This technique enables high-resolution imaging of the entire volume and therefore characterization of the bulk properties in a non-destructive way. The scans resulted in a voxel size of 27 μm^3. Propagation-based phase contrast was used to improve the contrast, which is a common approach for low-density samples where X-ray absorption is low. With increasing distance between the sample and detector, phase shifts caused by the refractive index of the sample are turned into detectable intensity variations, which results into a contrast improvement by applying a phase-retrieval algorithm.[42] We scanned 40 aerogels, ten for each condition, resulting in 40 3D volumes consisting of around 500 2D slices per volume. To enable quantitative analysis of the samples, all 40 volumes were normalized, and the carbon fibers were segmented. Porosity was defined by separation of the aerogel and air, followed by a local thickness filter, which fits spheres into the empty space of the aerogel. Porosity and local thickness were then analyzed in relation to their location in the volumes and their relative distance to the carbon fibers. We characterized the internal morphology of aerogels fabricated with the two freezing methods, for simplicity hereafter referred to as freezer-aerogels and liquid-N_2 aerogels. The mean porosity of the liquid-N_2 and freezer-aerogels without carbon fibers was very similar, 59% and 60% respectively (**Table 1**). On the other hand, in the samples that included carbon fibers the mean porosity of the liquid-N_2 aerogels was 68% while the porosity of the freezer-aerogels was 59%. So the integration of carbon fibers in the solution prior to liquid-N_2 freezing affected the pore formation resulting in 9% increase in mean porosity.

Table 1. Mean porosity of the freezer (F) and liquid-N_2 (N) aerogels with (w/CF) and without carbon fibers.

Sample	F w/CF	N w/CF	F	N
Mean porosity	0.59	0.68	0.60	0.59
Spread (FWHM)	50 μm	58.77 μm	42.03 μm	28.77 μm

The pore size distributions in all aerogel volumes showed pore radii mostly in the range of 15–50 μm, with the smallest detectable pore radius being 13.5 μm (limited by the 27 μm voxel size) (**Figure 2**E). The spread of radii values was evaluated by applying a Gaussian fit and extracting the FWHM (Full Width at Half Maximum). Freezer aerogels with and without carbon fibers had FWHM of 50 and 42 μm, respectively. The liquid-N_2 aerogels without fibers had smaller pores and a narrower pore distribution equal to 29 μm. When carbon fibers were embedded the spread in pore size almost doubled resulting in a FWHM of 59 μm. Typically, when the freezing temperature lowers and therefore the solidification velocity increases smaller pores are formed as the ice crystals freeze quickly without time to grow.[43] In our samples this was true for the aerogels without carbon fibers but not for the ones with carbon fibers where the liquid-N_2 aerogels had bigger pores than the freezer ones.

From CT scans of aerogels, the carbon fibers were segmented (Figure 2B and Video S1, Supporting Information) allowing us to assess how the carbon fibers impact the volume characteristics (**Figure 3**). The radial porosity distribution, that is, porosity as a function of the distance from the center of the volume toward the outer part of the aerogel, was homogeneous for the freezer-aerogels (Figure 3A). However, for the liquid-N_2 aerogels, the porosity is higher toward the center and drops toward the outer part of the aerogels. In terms of the pore size, the radial local thickness distribution, (local thickness is the size of the largest sphere fitted into the pore in pixels) is rather homogeneous for all aerogels except for the liquid-N_2 aerogels with carbon fibers (Figure 3B). We also observed an increase in porosity and local thickness at the outer edge of all aerogels, which may partly be attributed to pores not fully closed due to contact with the wall of the plastic mold. The carbon fibers had a preferred distribution, with more fibers toward the outside of the aerogels (Figure 3C). The effect of the carbon fibers on the aerogel morphology was evaluated by assessing how the porosity and local thickness change with the distance from the carbon fibers (Figure 3D,E). For the liquid-N_2 aerogels, porosity and local thickness overall increased with respect to the distance from the carbon fibers. In contrast for the freezer aerogels porosity and local thickness did not change significantly

Overall, the radial porosity and local thickness distribution of the liquid-N_2 aerogels had a significantly larger sample-to-sample

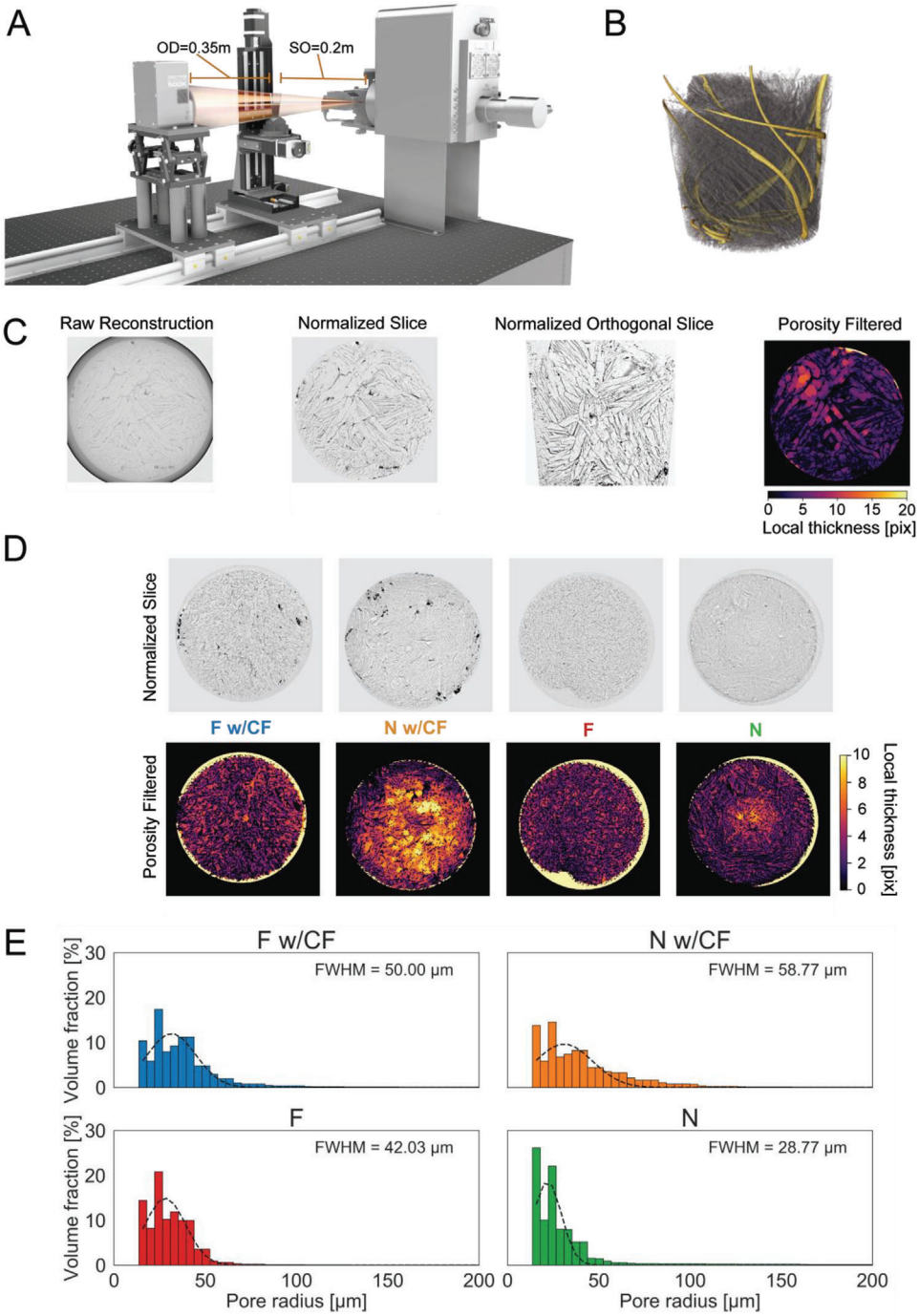

Figure 2. Aerogel X-ray microtomography setup and processing. A) Render of the X-ray microtomography setup with the source-object (SO) and object-detector (OD) distances marked. B) 3D render of the aerogel (grey) and the carbon fibers (gold) prepared using ORS Dragonfly software. C) Data processing of the reconstructed CT slices: a raw slice, a processed slice with normalizations and corrections applied, a normalized orthogonal slice along the height of the aerogel and a local thickness slice. D) Processed reconstructed slices from the different sample groups with their corresponding local thickness slices. E) Pore size distributions of the four different sample types with a Gaussian fit applied to extract the spread of values via the FWHM. F: freezer aerogel, N: Liquid-N_2 aerogel, w/CF: aerogels with embedded carbon fibers.

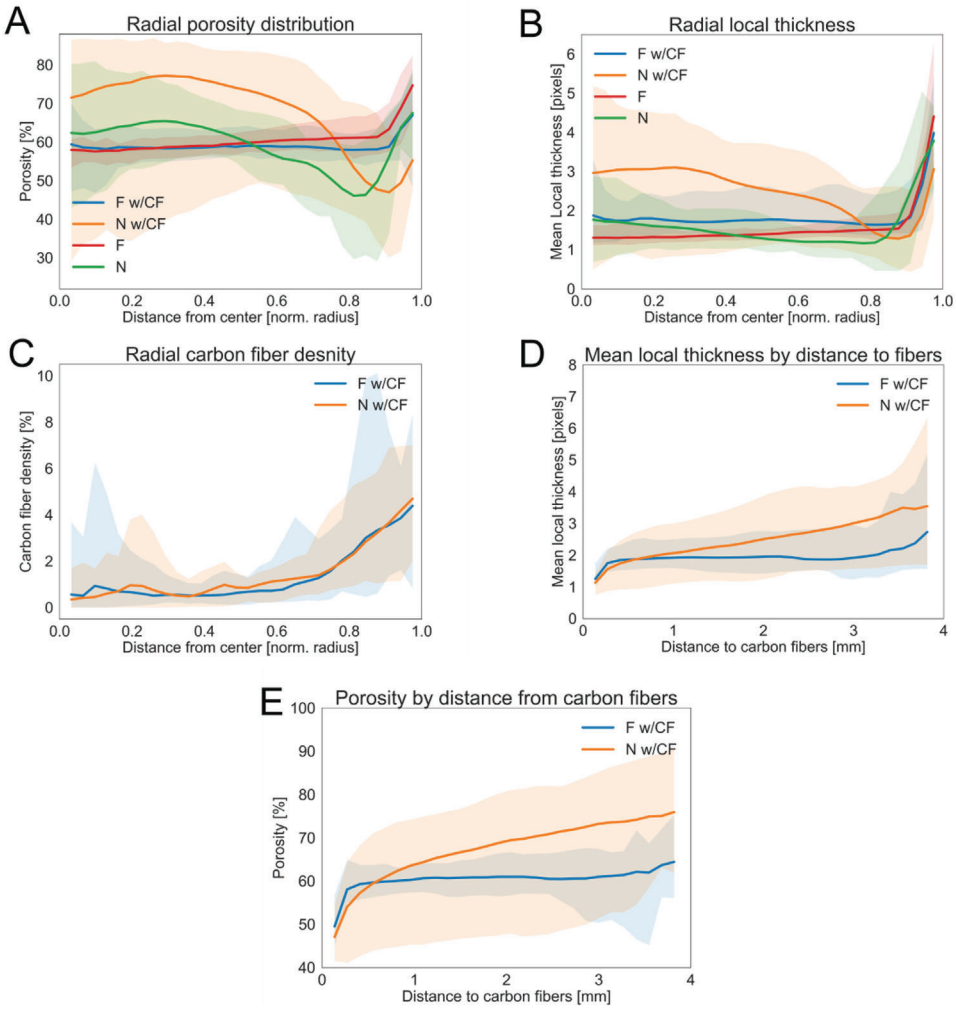

Figure 3. Porosity, pore size, and carbon fibers distributions. A) Radial porosity distribution: Porosity as a function of the distance from the center of the aerogel showing significant differences between the two freezing methods. B) Radial local thickness: Mean local thickness as a function of the distance from the center of the aerogel also showing differences between the two freezing methods. C) Radial distribution of carbon fibers in the volumes highlighting preferential locations of fibers toward the outer part of the aerogel. D) Mean local thickness as a function of distance from carbon fibers. E) Porosity as a function of distance from carbon fibers. An average of ten samples for each case with standard deviations is shown as the shaded part (standard deviation values are shown in Table S1, Supporting Information). F: freezer aerogel, N: Liquid-N_2 aerogel, w/CF: aerogels with embedded carbon fibers.

variation as compared to freezer-aerogels. The standard deviations, calculated for each corresponding data point in the respective sample group and then averaged over the full range of radii or distances, are significantly higher for the liquid-N_2 samples and are listed in Table S1 (Supporting Information). The total variation of values is shown in the background of the plots in Figure 3B–F. We speculate that the high variation between the liquid-N_2 samples arises from the fast freezing process where even slight changes may impact the ice crystal formation and eventually the porous structure.

Following the morphological analysis, we characterized the electrochemical properties of the aerogels with embedded carbon fibers with cyclic voltammetry in a three-electrode setup (**Figure 4**A). Cyclic voltammetry indicated that PEDOT:PSS and its electroactive character dominate the aerogel's electrochemical properties. We observed similar behavior for both freezing methods indicating that the difference in porosity between freezer-aerogels and liquid-N_2 aerogels as revealed by micro-CT did not significantly affect the charging characteristics. At low scan rates of 1 mV s^{-1} the charging is primarily capacitive within the voltage range of (−0.1, +0.5 V) (Figure 4A). This is consistent with the current understanding of PEDOT:PSS doping mechanism, which is largely influenced by the electrostatic interaction between ions and the electronic carriers on the PEDOT backbone.[44,45] When a negative voltage is applied to the aerogel relative to the electrolyte potential, PEDOT:PSS undergoes electrochemical reduction or dedoping. In this case, holes (polarons/bipolarons) are extracted from the polymer backbone and cations from the electrolyte are injected into the polymer matrix to compensate for the negative charges on the PSS and maintain the system's electroneutrality. On the contrary, when a positive voltage is applied, PEDOT is oxidized. During oxidation, holes

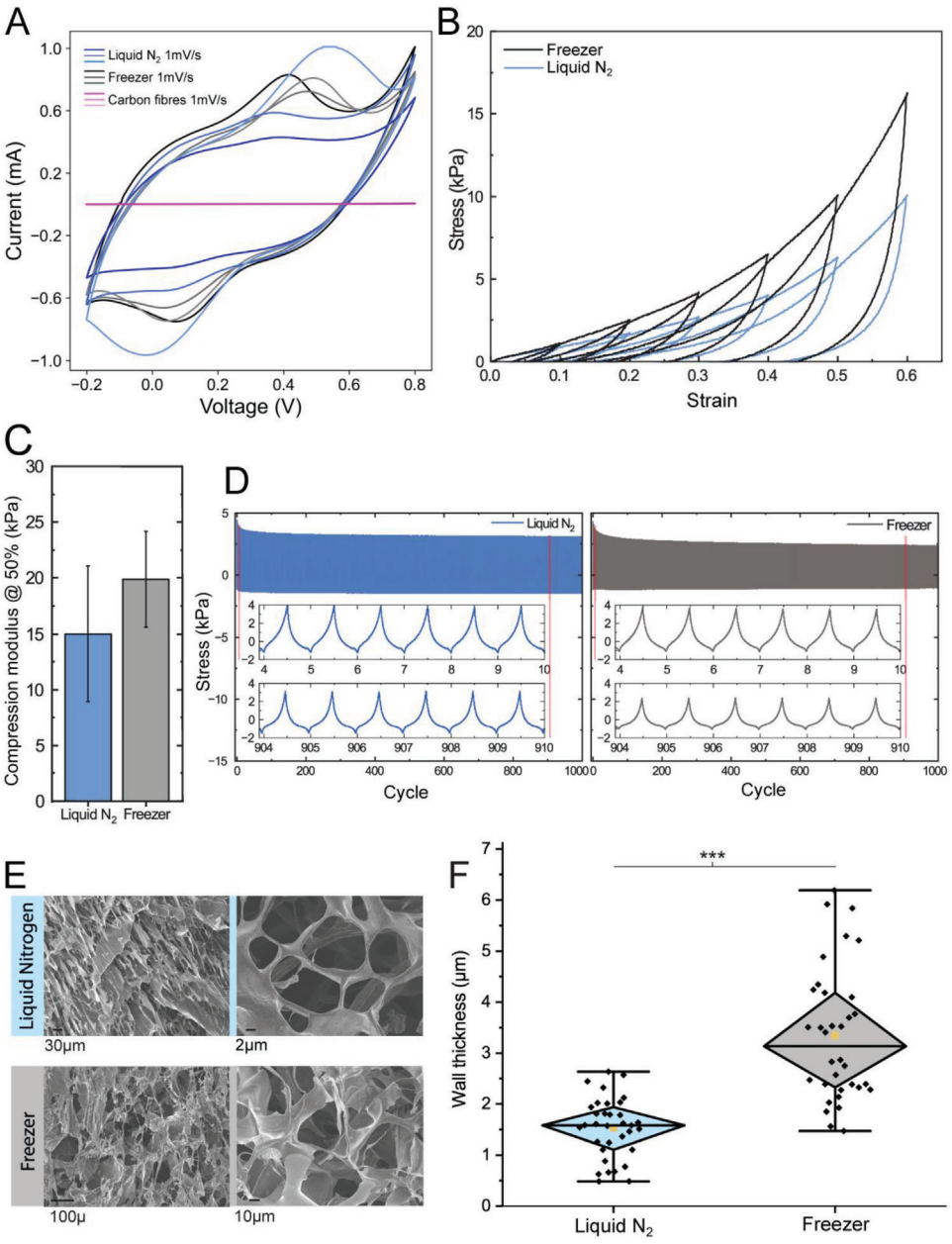

Figure 4. Electrochemical, mechanical, and SEM characterization of the aerogels. A) Cyclic voltammogram of different samples of freezer and liquid-N_2 aerogels with embedded carbon fibers and only carbon fibers at scan rate of 1 mV s^{-1} ($N = 3$ for each case). B) Compressive stress–strain curves for aerogels without carbon fibers at different strains. C) Compressive modulus of the liquid-N_2 and freezer aerogels at 50% compression, (n=5). D) Cyclic compression fatigue testing of the aerogels for 1000 cycles at 30% strain . E) SEM micrographs of cross sections showing how the morphology differs between the freezer and liquid-N_2 approach. F) Wall thickness of the aerogels based on SEM images showing significant difference between the two freezing methods ($N = 34$). (Mean value is depicted with yellow square and *** indicates a p value < 0.001).

are injected into the polymer backbone while cations are expelled and/or anions enter into the polymer matrix to balance the accumulated charges.[46] Particularly for the freezer aerogels peaks were present in the CV. Usually, peaks are attributed to faradaic processes in PEDOT.[47,48] However recent modeling studies argue toward purely electrostatic charging in PEDOT[44,49,50] where deviations from the ideal box shape in the CV may arise from limited electronic transport.[45] The cm^3 scale aerogels are addressed via the integrated carbon fibers resulting in different percolation paths between the addressing electrode and the PEDOT phase. This can induce inhomogeneities in the charge injection and transport along the PEDOT and consequently affect the charging processes.

Overall, there was a much larger sample to sample variation between the CVs of the liquid-N_2 aerogels, something that was also observed in their morphology. In addition, micro-CT revealed that porosity and the pore size distributions as a function of the distance from the carbon fibers varied also from sample to

sample and particularly for the liquid-N_2 aerogels something that can also affect the charging characteristics of the aerogel volume.

Then we proceed to evaluate the mechanical characteristics of the aerogels with linear compression. Aerogels without carbon fibers were compressed up to 60% of their length with 10% increments while monitoring the applied force (Figure 4B and Figure S2, Supporting Information). Typical stress–strain curves of cellular materials have three main regions; first a linear elastic region at low strains, second a plateau regime corresponding to the buckling of the cell walls where large deformation can occur with small stress, and a third region of densification where the cell walls crush together.[51] In the stress–strain curves of the freezer- and liquid N_2 aerogels (Figure 4B and Figure S2, Supporting Information), the buckling and densification regions are the most prominent and therefore we calculated the compression modulus of the aerogels at 50% strain. Freezer-aerogels had a higher compression modulus than liquid-N_2 aerogels with 20 and 15 kPa, respectively (Figure 4C). This trend was true for all tested strains with the compression modulus increasing with strain (Figure S2, Supporting Information) in agreement with the buckling and densification of the structure in higher strains[52,51] We also tested the mechanical stability of the aerogels with 30% compression fatigue loading over 1000 cycles. We found that the liquid-N_2 aerogels had better stability upon compression than the freezer ones with stress retention of 70% and 55%, respectively (Figure 4D).

The micro-CT analysis revealed that the mean porosity of the freezer and liquid-N_2 aerogels without fibers was similar. Liquid-N_2 aerogels had smaller pores than the freezer ones and according to the theory, this should result in a stiffer structure.[53] However, the liquid-N_2 aerogels were anisotropic with higher porosity and larger pores in the center and lower porosity, and smaller pores toward the outer part in comparison with the freezer aerogels. Furthermore, from the micro-CT contrast the liquid-N_2 aerogels appear to have thinner walls (Figure 2D and Figure S1, Supporting Information). To confirm that, we performed SEM imaging that has higher resolution than the micro-CT (Figure 4E). SEM revealed that indeed liquid-N_2 aerogels had thinner pore walls in comparison with freezer-aerogels (Figure 4E,F). Therefore, the increased compression modulus and less stability during cycling of the freezer aerogels can be a result of porosity, pore size, and wall thickness.

3. Conclusions

In this work, we characterized the bulk morphology of PEDOT:PSS-NFC aerogels with X-ray microtomography. The aerogels were fabricated with ice templating using two different freezing methods. Our analysis revealed that the freezing method did not impact the mean porosity of the aerogels without carbon fibers. However, when carbon fibers were integrated in the solution prior the freezing the resulting liquid-N_2 aerogels had higher porosity by 9%. Overall freezer aerogels were more homogeneous than liquid-N_2 ones that showed variation in radial porosity and radial pore size distributions. Median values of pore radii were ranging from about 15 to 50 μm for aerogels without carbon fibers and extended to larger values when carbon fibers were integrated. Liquid-N_2 aerogels without carbon fibers had smaller pores with narrower distribution but the ones with carbon fibers had by far the largest spread in pore sizes, up to two times larger radii than the other aerogels. Therefore, it is clear that the addition of carbon fibers into the mixture, in order to act as integrated electrodes, alters the morphology of the aerogel, especially when the freezing is fast. Overall liquid-N_2 aerogels had a much larger sample-to-sample variation in morphology characteristics; something that may arise from variations during the ice crystal formation.

The difference in porosity between freezer and liquid-N_2 aerogels with carbon fibers had no significant impact on their electrochemical properties signifying that charging of the PEDOT phase was not limited in the freezer aerogel that had lower porosity. However, there was an impact on the mechanical properties of the aerogels without carbon fibers, with the freezer aerogels having higher compression modulus than the liquid-N_2 ones. This can be explained by areas with larger pores and higher porosity present in the center of liquid-N_2 aerogels. Furthermore, SEM revealed that the freezer aerogels had thicker pore walls which can be a result of the slower freezing method that allows more solutes to concentrate during the formation of the ice crystals. The freezer aerogels were less stable in fatigue compression that can be due to the thicker pores walls that buckle and densify during compression and may have higher plastic deformation. Our work demonstrates that X-ray micro-CT is a powerful tool for characterizing the morphology of conducting cellulose based aerogels by giving detailed information on the distribution of porosity and pore size in the bulk of the aerogel and by enabling the visualization of integrated electrodes for addressing in a non-destructive manner. In contrast, mercury porosimetry, which is widely used for characterizing porous aerogels, is destructive, there are safety concerns over mercury use and it does not provide information in a spatially resolved manner.[39] Conducting cellulose aerogels can be used as active composites in many areas from energy to sensing and tissue engineering.[40,54] Particularly for tissue engineering applications, anisotropy on the pore size and porosity within the bulk of the scaffold can be important for the differentiation and proliferation of cells and the tissue formation.[55,56] Our work contributes to furthering the understanding of how the fabrication protocol impacts the structure and properties of the aerogels.

4. Experimental Section

Conducting Porous Aerogel Fabrication: PEDOT:PSS-NFC-GOPS aerogels were prepared as described before[37] with a few modifications. Briefly, PEDOT:PSS (PH1000, 1.3 wt% PEDOT:PSS, Heraeus Clevios), NFC (1 wt% carboxymethylated nanofibrillated cellulose, RISE Innventia), and GOPS (97 wt%, Alfa Aesar) in a ratio of 1:1:0.2, respectively, were homogenized with a disperser (IKA 3 386 000 ULTRA-TURRAX s). The mixture was poured into 30 mL polystyrene conical containers that contained ≈0.093 g carbon fibers with an average length of 12.5 cm that were randomly dispersed in the container. Freezer approach: The container was frozen at −20 °C for 24 h, followed by freeze-drying (BenchTop Pro, SP SCIENTIFIC) under −50 °C and 200 μbar for 72 h. Liquid Nitrogen approach: The container was immersed in liquid-N_2 at −196 °C for ≈10–15 s and until the samples were completely frozen, freeze-drying followed under −50 °C, and 200 μbar for 72 h. Freeze drying removes ice crystals resulting in the formation of a porous aerogel (Dimensions: Height = 2 cm, $Top_{diameter}$ = 1.5 cm, and $Bottom_{diameter}$ = 1 cm). The aerogels were then annealed at 140 °C for 30 min to enable the thermal crosslinking of PEDOT:PSS-NFC with GOPS. Finally, the aerogels were treated with DMSO vapor to enhance their

electrical conductivity. The aerogels were placed in a glass crystallized dish with a few drops of DMSO aside (1 mL), the Petri dish was capped and placed on a hot plate at 60 °C for 24 h.

Scanning Electron Microscopy: The freeze-dried aerogels (pieces of ≈1 cm in diameter) were attached to the sample holder with the help of copper tape. The SEM analysis took place with InLens lens of Zeiss-Sigma 500 Gemini SEM (2–2.5 kV), without any metal evaporation or sputtering. ImageJ was used for the wall thickness measurements.

X-Ray Micro-Tomography: X-ray microtomography scans were acquired with a custom laboratory system[57] consisting of a prototype solid anode micro-focus X-ray source (Excillum AB, Sweden) and a photon counting Eiger 2R 500K detector (Dectris Ltd., Switzerland) with a pixel size of 75 µm, placed 0.55 m from the source as depicted in Figure 2A. The X-ray spot was focused to 10 µm at 70 kV acceleration voltage with an emission power of 15 W. Samples were placed 0.2 m from the source, covering their full width, resulting in an effective pixel size of 27.27 μm^2, and a field-of-view of $\approx 28 \times 14$ mm^2.

Processing and Reconstruction: For each scan, 1080 projections over 360° were acquired with an exposure time of 2 s per projection. Prior to reconstruction, ring removal was applied using either a normalization or a median filter,[58] and phase retrieval was applied[42] with a delta/beta ratio of 350. Reconstructions were performed using the Feldkamp–Davis–Kress algorithm[59] via the ASTRA toolbox[60,61] in the Python programming language.

Normalization of the Volumes: The reconstructed 3D volumes were affected by unwanted biases. Image processing methods were used to reduce these biases (Figure 2A). A clear radial bias was observed, for which a correction procedure was defined. The first step of the procedure was to estimate a bias volume. It was assumed that the intensities of the aerogel cells were constant over the volume, so measuring this constant as a function of cylinder radius would give an estimate of the bias. It was found that the 80% pixel intensity quantile was a good estimate of the cell intensities over a larger subsection of the cylinder, which could include cell walls and noise. Thus, the 80% pixel intensity quantile as a function of cylinder radius was calculated. The resulting volume defined by these quantiles positioned on their respective radii was the bias estimate. A multiplicative bias model was used and therefore the original reconstructed intensities were divided by the quantiles resulting in an unbiased volume. Additionally, the reconstructions were cropped slightly at the top and bottom of the cylinder as the intensities varied with respect to the rest of the volume at the boundary, due to the X-ray cone beam geometry. A final normalization was done, where each volume was normalized by a linear affine transformation such that cross-comparisons were possible, that is, the intensity of cell walls, aerogel fibers, and air was comparable between volumes.

Segmentation of Aerogel and Fibers: To estimate the porosity of the aerogels, the cell walls were segmented from the volume. Bias removal made cell and cell wall intensities constant over the volume, which made it possible to do a simple threshold segmentation. The segmentation method was to filter the volume with a 3D Gaussian smoothing kernel to remove noise and then threshold the intensities at an appropriate value. The kernel standard deviation was chosen to be ≈1 pixel since walls were still clearly visible while removing as much noise as possible. Carbon fibers, when present, were segmented using the same approach. The standard deviation was, in this case, chosen to be larger with ≈3 pixels since this would blur most cell walls while keeping the denser fibers. Binary connected components resulting from this procedure were labeled as carbon fibers if they contained more than 10 000 pixels.

Measurements from 3D Volumes: Porosity is the measured ratio of empty and occupied space in the binarized volumes. To measure pore sizes and their distribution in the volume, a local thickness filter was applied (Figure 2D), which iteratively fits spheres into the empty space of the binarized volumes to find the largest possible sphere for each cell.[62] The structure of the aerogels was then assessed radially, by evaluating the porosity and local thickness depending on the radius, that is, the distance from the center of the volume (Figure 3A,B,D). Further, with the carbon fibers segmented, the same measures were extracted depending on the distance from the carbon fibers (Figure 3C,E).

Electrochemical Characterization: Cyclic voltammetry (CV) was performed on the aerogels and carbon fibers in 0.01 M KCl electrolyte (Sigma-Aldrich) at 1 mV s^{-1} scan rate, between −0.2 to 0.8 V using a metallic mesh as a counter electrode and an Ag/AgCl electrode as a reference electrode. All the measurements were performed at room temperature using a Gamry 1010E/B potentiostat.

Mechanical Characterization: Compression of the samples was performed using an in-house developed mechanical compression apparatus, consisting of a motorized X-LSQ300A-E01 linear stage (Zaber) and a force meter (M5-2, Mark-10) attached to it and controlled via LabView environment for data acquisition at a deformation rate of 12 mm min^{-1}.

The ratio of maximum mechanical stress to the corresponding strain was employed in the calculation of compression moduli ranging from 10% to 60%.

Statistical Analysis: Statistical analysis was carried out using the Origin 2020 software by a non-paired *t*-test. p values < 0.05 were considered significant.

Supporting Information

Supporting Information is available from the Wiley Online Library or from the author.

Acknowledgements

V.K.O. and T.D. contributed equally to this work. This work was supported by the Wallenberg Wood Science Center (KAW 2018.0452), the European Union's Horizon 2020 research and innovation programme under Grant Agreement No. 800926 (FET-OPEN-HyPhOE), the Swedish Research Council (VR-2017-04910) and (VR 2022–03507), and the Swedish Foundation for Strategic Research (ID17-0097 and FFL-18-0101). Additional funding was provided by the Swedish Government Strategic Research Area in Materials Science on Advanced Functional Materials at Linköping University (Faculty Grant SFO-Mat-LiU No. 2009-00971). The Capital Region of Denmark has supported the participation of the Center for Quantification of Imaging Data from MAX IV (QIM). Schematics in Figure 1 were created with BioRender.com.

Conflict of Interest

The authors declare no conflict of interest.

Data Availability Statement

The data that support the findings of this study are available from the corresponding author upon reasonable request.

Keywords

aerogels, cellulose, poly(3,4-ethylenedioxythiophene), X-ray microtomography

Received: April 10, 2023
Revised: September 29, 2023
Published online: November 1, 2023

[1] D. Klemm, B. Heublein, H. P. Fink, A. Bohn, *Angew. Chem., Int. Ed.* **2005**, *44*, 3358.

[2] M. A. Ashraf, S. Batool, M. Ahmad, M. Sarfraz, W. S. A. W. M. Noor, in *Biopolymers and Biotech Admixtures for Eco-Efficient Construction Materials*, ed. F. Pacheco-Torgal, V. Ivanov, N. Karak, H. Jonkers, Elsevier, New York **2016**, 1ed., Ch. 17.
[3] R. Bardet, J. Bras, in *Handbook of Green Materials*, ed. K. Oksman, A. P. Mathew, A. Bismarck, O. Rojas, M. Sain, World Scientific, Singapore **2014**, pp. 207–232.
[4] C. Felgueiras, N. G. Azoia, C. Gonçalves, M. Gama, F. Dourado, *Front. Bioeng. Biotechnol.* **2021**, *9*, 1.
[5] R. Akram, Natasha, S. Fahad, M. Z. Hashmi, A. Wahid, M. Adnan, M. Mubeen, N. Khan, M. I. A. Rehmani, M. Awais, M. Abbas, K. Shahzad, S. Ahmad, H. M. Hammad, W. Nasim, *Environ. Sci. Pollut. Res.* **2019**, *26*, 16923.
[6] M. Ilyas, W. Ahmad, H. Khan, S. Yousaf, K. Khan, S. Nazir, *Rev. Environ. Health* **2018**, *33*, 383.
[7] R. Pravalie, *Earth-Sci. Rev.* **2021**, *220*, 103689.
[8] T. Li, C. Chen, A. H. Brozena, J. Y. Zhu, L. Xu, C. Driemeier, J. Dai, O. J. Rojas, A. Isogai, L. Wågberg, L. Hu, *Nature* **2021**, *590*, 47.
[9] R. J. Moon, A. Martini, J. Nairn, J. Simonsen, J. Youngblood, *Chem. Soc. Rev.* **2011**, *40*, 3941.
[10] M. A. S. Azizi Samir, F. Alloin, A. Dufresne, *Biomacromolecules* **2005**, *6*, 612.
[11] E. Kontturi, P. Laaksonen, M. B. Linder, Nonappa, A. H. Gröschel, O. J. Rojas, O. Ikkala, *Adv. Mater.* **2018**, *30*, 1703779.
[12] T. Keplinger, X. Wang, I. Burgert, *J. Mater. Chem. A* **2019**, *7*, 2981.
[13] Z. Zhang, A. I. S. Ahmed, M. Z. Malik, N. Ali, A. Khan, F. Ali, M. O. Hassan, B. A. Mohamed, J. Zdarta, M. Bilal, *Chemosphere* **2023**, *313*, 137483.
[14] D. Zhao, A. Sultana, J. Edberg, M. Shiran Chaharsoughi, M. Elmahmoudy, U. Ail, K. Tybrandt, X. Crispin, *J. Mater. Chem. C* **2022**, *10*, 2732.
[15] S. Shariatnia, A. V. Kumar, O. Kaynan, A. Asadi, *ACS Appl. Nano Mater* **2020**, *3*, 5421.
[16] R. Brooke, M. Lay, K. Jain, H. Francon, M. G. Say, D. Belaineh, X. Wang, K. M. O. Håkansson, L. Wågberg, I. Engquist, J. Edberg, M. Berggren, *Polym. Rev.* **2022**, *63(2)*, 437.
[17] X. Wang, C. Yao, F. Wang, Z. Li, *Small* **2017**, *13*, 1702240.
[18] O. Eskilson, E. Zattarin, L. Berglund, K. Oksman, K. Hanna, J. Rakar, P. Sivlér, M. Skog, I. Rinklake, R. Shamasha, Z. Sotra, A. Starkenberg, M. Odén, E. Wiman, H. Khalaf, T. Bengtsson, J. P.E Junker, R. Selegård, E. M. Björk, D. Aili, *Mater. Today Bio* **2023**, *19*, 100574.
[19] M. A. Mohamed, M. Abd Mutalib, Z. A. Mohd Hir, M. F. M. Zain, A. B. Mohamad, L. J. Minggu, N. A. Awang, W. N. W. Salleh, *Int. J. Biol. Macromol.* **2017**, *103*, 1232.
[20] S. Dastidar, M. M. Alam, X. Crispin, D. Zhao, M. P. Jonsson, *Cell Rep. Phys. Sci.* **2022**, *3*, 101196.
[21] M. Liao, D. Banerjee, T. Hallberg, C. Åkerlind, M. M. Alam, Q. Zhang, H. Kariis, D. Zhao, M. P. Jonsson, *Adv. Sci.* **2023**, *10(8)*.
[22] S. Darabi, C. Y. Yang, Z. Li, J. Huang, M. Hummel, H. Sixta, S. Fabiano, C. Müller, *Adv. Electron. Mater.* **2023**, *9*, 2201235.
[23] C. Jia, C. Chen, Y. Kuang, K. Fu, Y. Wang, Y. Yao, S. Kronthal, E. Hitz, J. Song, F. Xu, B. Liu, L. Hu, *Adv. Mater.* **2018**, *30*, 1801347.
[24] B. D. Paulsen, K. Tybrandt, E. Stavrinidou, J. Rivnay, *Nat. Mater.* **2020**, *19*, 13.
[25] D. Zhao, Q. Zhang, W. Chen, X. Yi, S. Liu, Q. Wang, Y. Liu, J. Li, X. Li, H. Yu, *ACS Appl. Mater. Interfaces* **2017**, *9*, 13213.
[26] H. Du, M. Zhang, K. Liu, M. Parit, Z. Jiang, X. Zhang, B. Li, C. Si, *Chem. Eng. J.* **2022**, *428*, 131994.
[27] F. Jiao, A. Naderi, D. Zhao, J. Schlueter, M. Shahi, J. Sundström, H. Granberg, J. Edberg, U. Ail, J. Brill, T. Lindström, M. Berggren, X. Crispin, *J. Mater. Chem. A* **2017**, *5*, 16883.
[28] R. Brooke, J. Åhlin, K. Hübscher, O. Hagel, J. Strandberg, A. Sawatdee, J. Edberg, *J. Energy Storage* **2022**, *50*, 104191.
[29] A. Malti, J. Edberg, H. Granberg, Z. U. Khan, J. W. Andreasen, X. Liu, D. Zhao, H. Zhang, Y. Yao, J. W. Brill, I. Engquist, M. Fahlman, L. Wågberg, X. Crispin, M. Berggren, *Adv. Sci.* **2015**, *3*, 1500305.
[30] M. G. Say, C. J. Brett, J. Edberg, S. V. Roth, L. D. Söderberg, I. Engquist, M. Berggren, *ACS Appl. Mater. Interfaces* **2022**, *14*, 55850.
[31] S. Darabi, M. Hummel, S. Rantasalo, M. Rissanen, I. Öberg Månsson, H. Hilke, B. Hwang, M. Skrifvars, M. M. Hamedi, H. Sixta, A. Lund, C. Müller, *ACS Appl. Mater. Interfaces* **2020**, *12*, 56403.
[32] S. Han, F. Jiao, Z. U. Khan, J. Edberg, S. Fabiano, X. Crispin, *Adv. Funct. Mater.* **2017**, *27*, 1703549.
[33] S. S. Kim, J. H. Jeon, C. D. Kee, I. K. Oh, *Smart Mater. Struct.* **2013**, *22*, 085026.
[34] A. Y. Mehandzhiyski, I. Zozoulenko, *ACS Appl. Energy Mater.* **2019**, *2*, 3568.
[35] D. Belaineh, J. W. Andreasen, J. Palisaitis, A. Malti, K. Håkansson, L. Wågberg, X. Crispin, I. Engquist, M. Berggren, *ACS Appl. Polym. Mater.* **2019**, *1*, 2342.
[36] K. Jain, M. S. Reid, P. A. Larsson, L. Wågberg, *Carbohydr. Polym.* **2021**, *260*, 117818.
[37] S. Han, N. U. Alvi, L. Granlöf, H. Granberg, M. Berggren, S. Fabiano, X. Crispin, *Adv. Sci.* **2019**, *6*, 1802128.
[38] S. Han, T. P. Ruoko, J. Gladisch, J. Erlandsson, L. Wågberg, X. Crispin, S. Fabiano, *Adv. Sustainable Syst.* **2020**, *4*, 2000004.
[39] H. J. Haugen, S. Bertoldi, in *Characterization of Polymeric Biomaterials*, ed. M. C. Tanzi, S. Farè, Elsevier, New York **2017**, 1 ed., pp. 21–53.
[40] A. G. Guex, J. L. Puetzer, A. Armgarth, E. Littmann, E. Stavrinidou, E. P. Giannelis, G. G. Malliaras, M. M. Stevens, *Acta Biomater.* **2017**, *62*, 91.
[41] A. Håkansson, S. Han, S. Wang, J. Lu, S. Braun, M. Fahlman, M. Berggren, X. Crispin, S. Fabiano, *J. Polym. Sci., Part B: Polym. Phys.* **2017**, *55*, 814.
[42] D. Paganin, S. C. Mayo, T. E. Gureyev, P. R. Miller, S. W. Wilkins, *J. Microsc.* **2002**, *206*, 33.
[43] Y. Chen, L. Zhang, Y. Yang, B. Pang, W. Xu, G. Duan, S. Jiang, K. Zhang, *Adv. Mater.* **2021**, *33*, 2005569.
[44] A. V. Volkov, K. Wijeratne, E. Mitraka, U. Ail, D. Zhao, K. Tybrandt, J. W. Andreasen, M. Berggren, X. Crispin, I. V. Zozoulenko, *Adv. Funct. Mater.* **2017**, *27*, 1700329.
[45] K. Tybrandt, I. V. Zozoulenko, M. Berggren, *Sci. Adv.* **2018**, *1*, 1.
[46] M. O. Bamgbopa, J. Edberg, I. Engquist, M. Berggren, K. Tybrandt, *J. Mater. Chem. A* **2019**, *7*, 23973.
[47] M. Marzocchi, I. Gualandi, M. Calienni, I. Zironi, E. Scavetta, G. Castellani, B. Fraboni, *ACS Appl. Mater. Interfaces* **2015**, 7, 32, 17993-18003, https://doi.org/10.1021/acsami.5b04768.
[48] Q. Yang, S. K. Pang, K. C. Yung, *J. Electroanal. Chem.* **2014**, *728*, 140.
[49] I. Sahalianov, S. K. Singh, K. Tybrandt, M. Berggren, I. Zozoulenko, *RSC Adv.* **2019**, 42498, https://doi.org/10.1039/c9ra10250g.
[50] S. T. Keene, V. Gueskine, M. Berggren, G. G. Malliaras, K. Tybrandt, I. Zozoulenko, *Phys. Chem. Chem. Phys.* **2022**, 19144, https://doi.org/10.1039/d2cp02595g.
[51] M. F. Ashby, R. F. M. Medalist, *Metall. Trans. A* **1983**, *14*, 1755.
[52] T. A. Schaedler, A. J. Jacobsen, A. Torrents, A. E. Sorensen, J. Lian, J. R. Greer, L. Valdevit, W. B. Carter, *Science* **2011**, *334*, 962.
[53] E. Segreto, *Phys. Rev. D* **2021**, *103*, 43001.
[54] C. M. Moysidou, C. Pitsalidis, M. Al-Sharabi, A. M. Withers, J. A. Zeitler, R. M. Owens, *Adv. Biol.* **2021**, *5*, 2000306.
[55] E. Zeglio, A. L. Rutz, T. E. Winkler, G. G. Malliaras, A. Herland, *Adv. Mater.* **2019**, *31*, 1806712.
[56] C. Pitsalidis, A. M. Pappa, A. J. Boys, Y. Fu, C. M. Moysidou, D. Van Niekerk, J. Saez, A. Savva, D. Iandolo, R. M. Owens, *Chem. Rev.* **2022**, *122*, 4700.
[57] T. Dreier, N. Peruzzi, U. Lundström, M. Bech, *Appl. Opt.* **2021**, *60*, 5783.

[58] N. T. Vo, R. C. Atwood, M. Drakopoulos, *Opt. Express* **2018**, *26*, 28396.
[59] L. A. Feldkamp, L. C. Davis, J. W. Kress, *J. Opt. Soc. Am. A* **1984**, *1*, 612.
[60] W. Van Aarle, W. J. Palenstijn, J. De Beenhouwer, T. Altantzis, S. Bals, K. J. Batenburg, J. Sijbers, *Ultramicroscopy* **2015**, *157*, 35.
[61] W. Van Aarle, W. J. Palenstijn, J. Cant, E. Janssens, F. Bleichrodt, A. Dabravolski, J. De Beenhouwer, K. J. Batenburg, J. Sijbers, *Opt. Express* **2016**, *24*, 25129.
[62] J. Gostick, Z. Khan, T. Tranter, M. Kok, M. Agnaou, M. Sadeghi, R. Jervis, *J. Open Source Softw.* **2019**, *4*, 1296.